Fire Safety Journal 152 (2025) 104344

Contents lists available at ScienceDirect

Fire Safety Journal

journal homepage: www.elsevier.com/locate/firesaf

The influence of small mass loss rate peaks on the rate of spread of predictive flame spread simulations: A theoretical study

Tássia L.S. Quaresma [a], Tristan Hehnen [b], Lukas Arnold [a,b,*]

[a] Institute for Advanced Simulation, Forschungszentrum Jülich, Wilhelm-Johnen-Straße, 52428 Jülich, Germany
[b] Chair of Computational Civil Engineering, University of Wuppertal, Pauluskirchstraße 7, 42285 Wuppertal, Germany

ARTICLE INFO

Dataset link: https://doi.org/10.5281/zenodo.12804448

Keywords:
Pyrolysis modelling
Predictive flame spread simulation
Rate of spread
Computational fluid dynamics (CFD)
Fire dynamics simulator (FDS)
Thermogravimetric analysis (TGA)
Poly(methyl methacrylate) (PMMA)
Sensitivity analysis

ABSTRACT

Peaks in the mass loss rate (MLR) curve derived from thermogravimetric analysis (TGA) are commonly used to infer the pyrolysis rates of solid fuels. While the main peaks are often modelled, smaller MLR fluctuations are typically neglected, leading to discrepancies between models and experiments. The impact of these small fluctuations on key simulation predictions, however, remains unclear. This study systematically explores a specific scenario in which a small MLR fluctuation significantly affects the predicted rate of spread (ROS) of a simplified flame spread simulation. The MaCFP-recommended pyrolysis model for poly(methyl methacrylate) (PMMA) is adapted to incorporate a small MLR peak accounting for 0.5 % to 2 % of the sample's total mass. Results from sensitivity analyses show that the peak position has the greatest impact on the ROS, followed by the peak mass fraction, while the peak width has negligible effect. Adding a small peak at lower temperatures increased the ROS by up to 6 % to 13 %, depending on the peak's mass fraction, whereas peaks at higher temperatures had little to no effect. These results indicate that fluctuations at lower temperatures, w.r.t. the main peak, could significantly enhance the predicted spread rates and should be considered in flame spread simulations.

1. Introduction

1.1. Motivation

A key aspect in developing predictive flame spread simulations is modelling the pyrolysis of solid fuels. This requires accounting for the heat transfer within the solid material as well as the pyrolysis reactions and their respective rates. Determining the rates of pyrolysis is particularly important for materials whose pyrolysates contain a high yield of combustible gases. In such cases, the pyrolysis rates dictate the speed at which combustible gases are produced and supplied to the gas phase for combustion, consequently influencing the heat release rates (HRRs) from the fire [1]. The HRR affects the heat flux that heats the solid material, creating a feedback loop that sustains the flame spread process.

Common engineering approaches to determining pyrolysis rates involve analysing mass loss rates (MLRs) derived from thermogravimetric analysis (TGA) measurements. Peaks in the MLR curve are interpreted as representing pyrolysis reactions, with the associated reaction rates typically modelled using the Arrhenius equation. However, pyrolysis models rarely capture the full complexity of MLR measurements, often neglecting small fluctuations in the data. This happens for at least two reasons: (i) the number of modelled reactions is limited for practical purposes, despite experimental data often suggesting the presence of additional reactions; and (ii) experimental data can be inconsistent, showing variability in individual measurements or discrepancies across different apparatuses [2].

It is often assumed that neglecting the uncaptured MLR fluctuations in pyrolysis models has little to no effect on flame spread simulation predictions. This paper aims to challenge that assumption by demonstrating a specific scenario where these neglected fluctuations have a significant influence on flame spread predictions. While this study focuses on a single example, it raises the possibility that many other scenarios could be similarly affected – a hypothesis that justifies further investigation in future, more comprehensive studies.

The scenario considers horizontal flame spread over a PMMA sample, using an established pyrolysis model that accounts for two decomposition reactions. An additional reaction representing a small MLR peak is introduced to the model, and its impact on the predicted rate of spread (ROS) is evaluated. The analysis follows a two-step approach: (i) identifying positions where the original model deviates

* Corresponding author at: Institute for Advanced Simulation, Forschungszentrum Jülich, Wilhelm-Johnen-Straße, 52428 Jülich, Germany.
E-mail addresses: t.quaresma@fz-juelich.de (T.L.S. Quaresma), hehnen@uni-wuppertal.de (T. Hehnen), l.arnold@fz-juelich.de, arnold@uni-wuppertal.de (L. Arnold).

https://doi.org/10.1016/j.firesaf.2025.104344
Received 27 August 2024; Received in revised form 7 December 2024; Accepted 11 January 2025
Available online 31 January 2025

from experimental MLR data and adding the new reaction accordingly, and (ii) systematically assessing the effect of the additional reaction across the entire pyrolysis range.

The influence of the small MLR peak on ROS is explored using two methodologies. First, a one-at-a-time sensitivity analysis isolates the effects of the peak's position, mass fraction, and width. Second, a global sensitivity analysis employing Sobol indices [3] and polynomial chaos expansion (PCE) [4] quantifies the relative importance of these parameters across the full parameter space, offering a more robust understanding of their influence.

1.2. PMMA pyrolysis

Different reaction schemes have been proposed for modelling PMMA pyrolysis based on the MLR curve profile. These differences involve not only the number of identified MLR peaks but also the serial or parallel nature of the defined pyrolysis reactions. In some studies, PMMA pyrolysis is very simplified, being described by a single reaction representing the main MLR peak [5,6]. Other approaches built on cast PMMA data account for two reactions, which can be either in series [7] or in parallel [8,9]. In these models, the first reaction represents a smaller MLR peak observed at lower temperatures, while the second represents the main peak at higher temperatures. Furthermore, comparison against the utilised TGA data shows that in these cases only the most significant MLR peaks were modelled, while small peaks were neglected. Exceptions to this trend are, for example, the works of Ferriol et al. [10] and Hehnen and Arnold [11], where a general framework of multiple parallel reactions was proposed as a strategy to achieve thorough representation of the total MLR data.

The MLR data itself can exhibit significant variability due to several factors. For PMMA, these include the polymerisation method used (e.g. free radical initiation, anionic initiation [12,13]), the manufacturing process (e.g. extruded, cast [7]), the molecular weight [10], samples provided by different vendors, experimental conditions, material colour, sample preparation [14], device calibration, and might even vary depending on the utilised TGA apparatus [2]. Moreover, the application of smoothing techniques to reduce noise in MLR data can result in loss of information and potentially lead to inaccurate representation of the real MLR behaviour [15].

For each peak identified in the MLR curve representing a pyrolysis reaction, kinetic parameters – the pre-exponential factor (A) and the activation energy (E) – need to be estimated. Various methods can be used for this estimation, including analytical methods (e.g., conventional, direct differential) and curve-fitting optimisation methods [16,17]. This study is in the context of the latter approach, which combines pyrolysis models with optimisation algorithms in an inverse modelling technique to determine A and E [5,7,11,18]. Defining the optimisation strategy involves selecting an appropriate optimisation algorithm [19], target data, as well as a cost function [20].

In this study, particular attention is paid to the pyrolysis scheme proposed by Fiola et al. [7], as it is the current recommendation of the MaCFP working group for modelling PMMA pyrolysis [21]. Within MaCFP, this model is referred to as the UMD Pyrolysis Model, but for brevity, it will hereafter be called the UMD Model. The UMD Model was constructed based on TGA data for black cast PMMA [21], which exhibits small MLR peaks at lower temperatures followed by a large main peak. The scheme accounts for two first-order reactions: one representing a minor peak at approximately 190 °C and another corresponding to the main peak at around 374 °C. The model assumes that the first peak arises from the release of solvent trapped within the polymer matrix. However, the small peak is also designed to represent the melted polymer ($PMMA_{melt}$), which reacts to form an intermediate solid ($PMMA_{int}$). This intermediate solid then undergoes further reactions, releasing most of the combustible gases ($PMMA_{gas}$).

Previous TGA studies on PMMA thermal degradation under nitrogen atmosphere and varying heating rates have attributed small, low-temperature peaks to the volatilisation of impurities, such as residual monomer or additives [13,22]. However, other research attributes these peaks to the onset of depolymerisation, triggered by the breaking of weak linkages at the polymer chain ends – a behaviour particularly common in radically polymerised PMMA [10,23–25]. The scheme proposed by Fiola et al. [7] aligns more closely with the latter explanation, even though it appears to have been originally built on the former. It is important to note, however, that in practical applications, especially in fire modelling, pyrolysis models are primarily developed to estimate the rates at which combustible gases are released into the gas phase for combustion, rather than to replicate the precise chemical mechanisms occurring during pyrolysis. Therefore, due to the employed simplifications, the utilised pyrolysis scheme is considered an effective model.

The UMD Model formulation, with two serial reactions, leads to an apparent overall good agreement with the total MLR from TGA experiments [7]. However, a closer inspection of the MLR *vs.* temperature plot reveals small deviations from the experimental data across the entire pyrolysis range. These deviations are particularly noticeable at the shoulders of the main peaks, where fluctuations in the experimental MLR data are not captured by the original model. Typically, such fluctuations are assumed to have negligible impact on model predictions of interest, such as the rate of spread (ROS), and are therefore often disregarded. However, the extent to which overlooking these fluctuations influences the variability in flame spread simulations, particularly in predicting the ROS, remains unclear.

Only few previous studies have focused on understanding the impact of kinetic parameters and material properties on predictive models that particularly involve flame spread [26,27]. Specifically, hardly any studies have addressed the effect of using different kinetic schemes for modelling PMMA pyrolysis, let alone the impact of accounting for small MLR peaks. Bal and Rein [28] investigated the effect of using different kinetic schemes on ignition times, considering single- and multiple-step reactions. Their study suggested that a single-step mechanism would be sufficient to represent the material behaviour, due to the secondary importance of kinetics in comparison to the heat transfer in the solid. Fiola et al. [7] performed in their study a simplified sensitivity analysis to compare pyrolysis properties of extruded and cast PMMA for modelling gasification experiments. Among other differences, the two sets of properties differed by the number of peaks identified in TGA/microscale combustion calorimeter (MCC) experiments. Their study concluded that pyrolysis properties of extruded and cast PMMA can be used interchangeably. However, the study by Fiola et al. is focused on micro-scale, i.e. Simultaneous Thermal Analysis (STA) as well as MCC [29], and bench-scale, i.e. the Controlled Atmosphere Pyrolysis Apparatus II (CAPA II) [30], setups where no flame spread takes place. It could be demonstrated that individual parameters exhibit different sensitivities from micro- and bench scale to setups where self-sustained flame spread occurs [31]. Thus, further research is needed to assess how uncertainties in pyrolysis models directly affect the predictions of flame spread models.

2. Methods

2.1. Numerical modelling of flame spread

The simulation setup was designed to enable a steady-state, self-sustained flame spread on a horizontal PMMA plate of bench-scale dimensions. The Fire Dynamics Simulator (FDS) [32], version FDS6.7.9-0-gec52dee-HEAD, was selected as the modelling framework. An overview of the most refined case is presented in Fig. 1 for illustration purposes. The numerical model was developed to serve as a simplified sandbox case to apply state-of-the-art approaches for predicting flame spread within FDS. Key aspects of the solid-phase definition, including sample dimensions, material properties, and pyrolysis kinetics, were tailored to replicate the characteristics of black cast PMMA, consistent

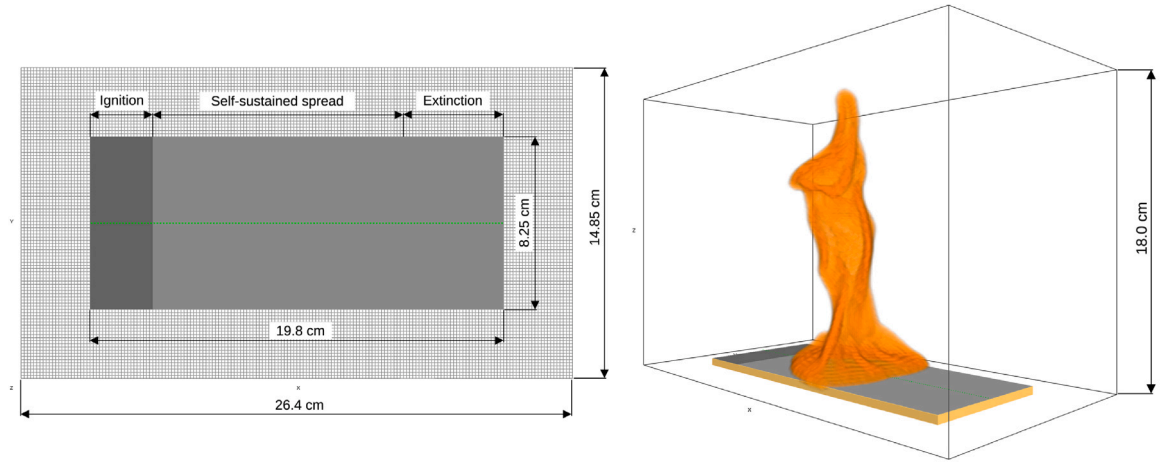

Fig. 1. Simulation setup of a self-sustained flame spread over a horizontal PMMA sample. The most refined case is shown, consisting of 1.5 mm gas phase cells. (a) Top view showing dimensions, gas phase grid, and zones of spread; (b) perspective view showing a self-sustained spreading flame.

with the material used in the MaCFP studies.

The sample thickness is set to 6 mm. Width and length of the sample were assigned to have approximately 100 mm and 200 mm, respectively. The values of width and length were slightly adjusted to conform with the tested gas phase cell sizes. An external heat flux of 65 kW m^{-2} is applied to one of the sample ends for 100 s to start ignition. The dark grey patch in Figs. 1(a) and 1(b) extends for 30 mm in the x-direction, indicating the region where the sample is ignited.

Zones of spread were defined as depicted in Fig. 1(a), such that the influences of the ignition and the end of the sample were excluded from the self-sustained spread phase. Fig. 1(a) shows a row of green dots along the sample's central line, indicating devices that capture the HRR per unit volume (HRRPUV) from the gas phase cells just above the sample. Using the methodology proposed by Quaresma et al. [31], the cell with the maximum HRRPUV is used as criterion to represent the flame leading edge. The position of the leading edge is then monitored throughout the simulation. From this information, the ROS is calculated as the first derivative of the function describing the relation between flame position and simulation time. The calculated ROS refers only to the region with self-sustained spread, thereby excluding the effects of ignition and extinction zones.

The back side of the sample is insulated with a board of Marinite 20 mm thick, whose width and length correspond to those of the sample. No wind or forced ventilation conditions were considered. Further details on the modelling of the solid and gas phases, as well as details on grid analyses and other simulation settings are provided in the following subsections.

2.1.1. Solid phase

The rates at which the solid material looses mass due to pyrolysis were defined to vary exponentially with the local temperatures of the solid, as established by the Arrhenius equation [32,33]. In general, four input parameters are required to define a rate of reaction: the pre-exponential factor A, the activation energy E, the mass fraction of the solid, and the order of reaction. Alternatively, in FDS, a pyrolysis reaction can be defined in terms of the parameters `PYROLYSIS_RANGE` (ΔT), `REFERENCE_TEMPERATURE` (T_p), and `HEATING_RATE` ($\dot{T}$) instead of A and E. The parameter ΔT refers to the width of the peak, assuming its shape to be approximately triangular, whereas T_p is simply the peak temperature. From ΔT and T_p, FDS calculates A and E using the following relations:

$$r_p = \frac{2\dot{T}}{\Delta T} Y_\mathrm{s}(0)\left(1-\nu_\mathrm{s}\right) \tag{1}$$

$$E = \frac{\mathrm{e} r_p}{Y_s(0)} \frac{RT_p^2}{\dot{T}} \tag{2}$$

$$A = \frac{\mathrm{e} r_p}{Y_s(0)} \exp\left(\frac{E}{RT_p}\right) \tag{3}$$

where r_p is the peak reaction rate, $\dot{T}$ is the heating rate used in the TGA experiment, $Y_s(0)$ is the initial mass fraction of the solid, and ν_s is the yield of the solid residue [32]. In the scope of this work, the pyrolysis reactions will be described and discussed in terms of ΔT and T_p, as performed in previous inverse modelling studies by Hehnen and Arnold [11], and Lauer et al. [9]. This approach allows for a direct representation of the MLR peaks within the pyrolysis temperature ranges of interest, making sampling more efficient and representative of the behaviour of real materials. That is because directly sampling E and A can produce unrealistic reaction rates. This risk arises because the sampling space for A is extremely large, and the exponential sensitivity of the model to E can amplify small variations, creating unreasonably high reaction rates. By contrast, T_p and ΔT provide a more intuitive and direct link to the MLR curve when visualised, ensuring that the sampled values align well with the expected physical behaviour.

In this contribution, the reaction scheme describing PMMA pyrolysis was built on the formulation proposed by Fiola et al. [7] for cast black PMMA. This formulation was particularly chosen because it provides the set of kinetic parameters and material properties which are recommended by the MaCFP working group for modelling PMMA pyrolysis [21]. The recommendation is based on validation exercises conducted in 2023 that defined the best performing parameter set as the one which closest predicted MLR measurements produced with the NIST Gasification Apparatus. In addition, the parameter set has been employed before to simulate real-scale flame spread experiments, as the Single Burning Item (SBI) setup [26], the Parallel Panels Test during the 2023 MaCFP workshop (MaCFP-3), and is part of the FDS validation suite [34].

Fig. 2 presents the UMD Model alongside the experimental normalised residual mass (Fig. 2(a)) and the MLR curve (Fig. 2(b)). The experimental curves were obtained by averaging TGA data reported by several different institutes to the MaCFP database (namely NIST, TIFP, UMD, and UQ), ensuring that the data more accurately reflects the real material behaviour and accounts for potential variability in experimental conditions. The experiments were conducted using a heating rate of 10 K/min and nitrogen atmosphere, resulting in MLR profiles where small peaks at low temperatures and a large peak at

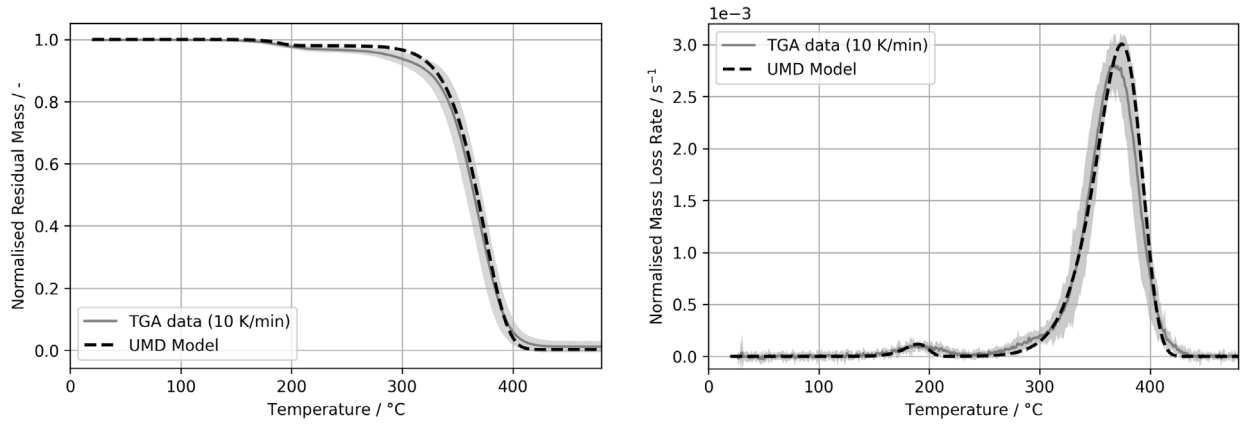

(a) (b)

Fig. 2. Comparison of the original model (UMD Model [7], reference model for PMMA pyrolysis) with TGA data from the MaCFP Database [21]. The experimental data represents the average of multiple datasets provided by NIST, TIFP, UMD, and UQ. (a) Normalised residual mass; (b) Mass loss rate.

high temperatures can be observed. The kinetics of PMMA pyrolysis in this model are represented by two serial first-order reactions, capturing two main peaks observed in Fig. 2(b). The first reaction (here named R1) was introduced to represent a small MLR peak observed at approximately 190 °C in Fig. 2(b). It was described considering that the melted polymer ($PMMA_{melt}$) produces 2 % of a combustible gas ($PMMA_{gas}$), and 98 % of an intermediate component ($PMMA_{int}$). It was then assumed that the production of $PMMA_{int}$ triggers a secondary pyrolysis reaction (R2), which in turn produces 0.2 % of char and 99.8 % of the same combustible gas as in reaction R1, $PMMA_{gas}$. The kinetic parameters A and E were determined by inverse modelling, using data of TGA experiments as target. Data of DSC measurements were used to determine the heats of reaction of R1 and R2, as well as the material specific heat capacity, as described elsewhere [7,35]. The reactions R1 and R2 are shown in , and their respective kinetic parameters and heats of reaction are presented in Table 2.

The pyrolysis scheme in the UMD Model, defined by reactions R1 and R2, captures the main MLR peaks observed in the variability of the experimental data, as shown in Fig. 2. However, they are insufficient to account for smaller additional MLR peaks or fluctuations observable throughout the temperature range where PMMA pyrolyses. As a consequence, the total MLR obtained with the two-reaction UMD Model deviates from the MLR derived from TGA experiments. Some of these deviations can be observed, for example, in the 210 °C to 310 °C range, and above 400 °C, as indicated by the red arrows in Fig. 3. Additionally, a significant deviation from the experimental data is observed at the main peak associated with reaction R2. The model displays a higher MLR peak than the average experimental data, with a slight shift towards higher temperatures. Assuming that all pyrolysis reactions of PMMA are of first-order, such deviations in the total MLR can only be reduced if more pyrolysis reactions are included in the model.

On this basis, a third parallel reaction (R3) is introduced to represent a small peak that is not accounted for by the UMD Model. R3 is defined to yield 0.2 % of char and 99.8 % of $PMMA_{gas}$, similar to reaction R2, as shown in . As an example, the peak temperature of reaction R3 was set to $T_p = 210\,°C$, and its pyrolysis range, i.e. peak width, was set to $\Delta T = 80\,°C$. However, considering the regions indicated by the red arrows in Fig. 3, there are several possible combinations of peak temperature, pyrolysis range, and mass fractions that can characterise a small peak to improve agreement with the experimental data. Understanding how this variability in the R3 peak affects the ROS is the main objective of this study, and will be addressed in detail later in the text.

Heat transfer inside the solid was considered to occur only in the direction perpendicular to the sample surface. Hence, the default 1-D conduction model available in FDS was selected. Spatial discretisation of the PMMA layer was set to uniform, whereas the default stretched node spacing for the layer of the insulation material was adopted. The parameter controlling the solid phase discretisation `CELL_SIZE_FACTOR` was set to 1.0, as it was found that values lower than unity (0.1, 0.5), which lead to increased resolution, had negligible effects on the ROS, while significantly increasing the computational cost. This setting produced 18 nodes spaced by 0.35 mm in the PMMA layer, and 10 stretched nodes in the layer of the insulation material. It is important to note that as the thickness of the sample is reduced due to thermal decomposition, the nodes are automatically rearranged by FDS during the simulation.

Thermophysical and optical parameters describing the PMMA sample in the UMD Model follow the specifications proposed by Fiola et al. [7]. Both $PMMA_{melt}$ and the residue $PMMA_{char}$ were described by the same set of properties. For consistency, here $PMMA_{imp}$ is also described using these properties. The set of material properties includes sample emissivity, absorption coefficient, density, thermal conductivity and specific heat capacity. The thermal conductivity and the specific heat capacity are given as temperature-dependent parameters, determined by piecewise linear functions. The values for sample emissivity, absorption coefficient, and density are 0.96, $2870\,m^{-1}$, and $1210\,kg\,m^{-3}$, respectively. For associated uncertainties and details on the estimation procedure to obtain these parameters, the reader should refer to the original work of Fiola et al. [7].

The material definition used for the insulation board was taken from the Parallel Panel simulation setup by NIST, which is publicly available in the FDS validation repository [36]. The properties correspond to those of Marinite, a common insulating material in fire experiments. The density and emissivity of Marinite were set to $737\,kg\,m^{-3}$ and 0.90, respectively. The thermal conductivity and specific heat capacity were assumed to be constant at $0.12\,W\,m^{-1}\,K^{-1}$ and $1.20\,kJ\,kg^{-1}\,K^{-1}$, respectively.

2.1.2. Gas phase

The combustible gas $PMMA_{gas}$ produced by the defined pyrolysis reactions was described with the properties of the monomer methyl methacrylate (MMA). The combustion of MMA was assumed to be mixing-controlled, and the Large Eddy Simulation (LES) mode was selected. In FDS, the LES simulation mode refers not only to the turbulence modelling, but also to a set of other sub-models describing, for example, flame extinction and wall models. All default settings within this simulation mode were applied, including the Deardorff model for sub-grid scale eddy viscosity, and the wall-adapting local eddy-viscosity (WALE) model for near-wall turbulence. The default radiation model based on the grey gas assumption was used, which assumes an optically

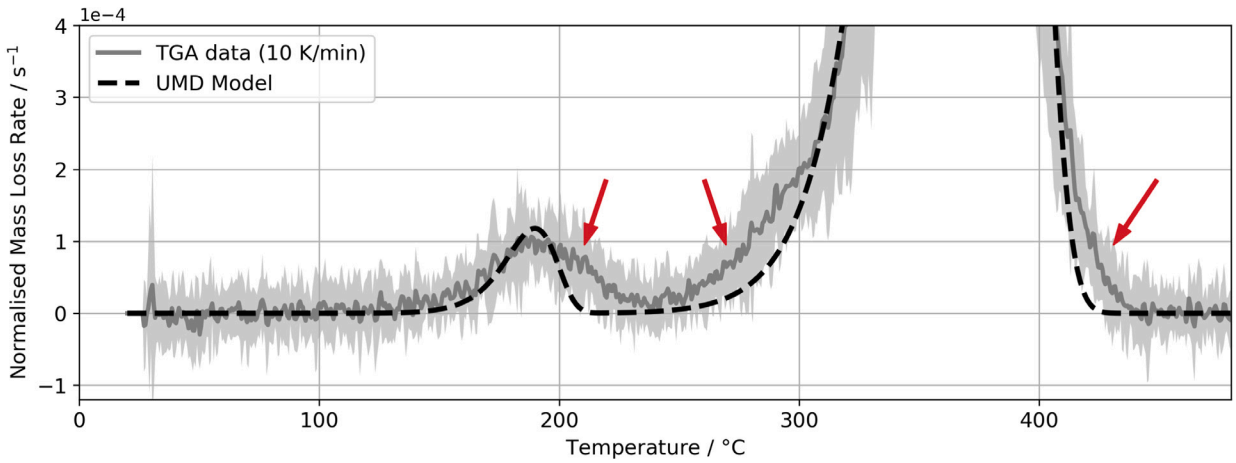

Fig. 3. Zoomed-in view of the mass loss rate curve, emphasising the deviations between the original UMD Model and the experimental average data (indicated by the red arrows). (For interpretation of the references to colour in this figure legend, the reader is referred to the web version of this article.)

Table 1
Scheme of reactions representing PMMA pyrolysis.

Label	Pyrolysis reactions	Source
R1	$PMMA_{melt} \rightarrow 0.98\ PMMA_{int} + 0.02\ PMMA_{gas}$	UMD Model, by Fiola et al. [7]
R2	$PMMA_{int} \rightarrow 0.002\ PMMA_{char} + 0.998\ PMMA_{gas}$	
R3	$PMMA_{imp} \rightarrow 0.002\ PMMA_{char} + 0.998\ PMMA_{gas}$	This work

Table 2
Kinetic parameters and heats of reaction of PMMA pyrolysis reactions, R1 and R2 from Fiola et al. [7].

Label	A $/s^{-1}$	E $/J \cdot mol^{-1}$	Peak temperature $(T_p)/°C$	Pyrolysis range $(\Delta T)/°C$	Heat of reaction $/kJ \cdot kg^{-1}$
R1	4.95e+16	1.64e+05	189.95	59.0	5.0
R2	1.35e+11	1.64e+05	374.3	115.3	817.0
R3	2.06e+12	1.32e+05	210.0	80.0	5.0

thick flame. A specified radiative fraction determines the portion of the total heat released as thermal radiation.

Thermophysical properties of MMA and the yields of its combustion products follows the description used in the Parallel Panel validation cases by NIST [34]. The specific heat capacity of MMA was fixed at $1.10\,kJ\,kg^{-1}\,K^{-1}$, and its thermal conductivity and diffusivity were calculated by FDS from the prescribed Lennard-Jones parameters $\sigma = 4.701$ Å, and $\epsilon/k = 205.78$ K. The yields of soot and CO were assigned respectively to 0.022 and 0.01. Based on the chemical formula of MMA ($C_5H_8O_2$), and the specified yields of soot and CO, the heat of combustion is given as $24\,265.3\,kJ\,kg^{-1}$. The radiative fraction of the MMA gas is set to 0.31.

A grid sensitivity study was carried out with different gas phase cell sizes: 3.0, 2.5, 2.0, and 1.5 mm. It was observed that a stable self-sustained spread did not occur for cell sizes larger than 2.0 mm, as the flame extinguished soon after the end of ignition. In the 2.5 mm case, although propagation towards the end of the sample was observed, the flame assumed an asymmetrical and unstable shape along the way. For each of the 1.5, 2.0, and 2.5 mm cases, the impact on the ROS due to the number of radiation angles (NRA) was evaluated. Three values of NRA (104, 1208, 3016) were tested, and it was found that the effect of the NRA was insignificant across all gas phase resolutions. In light of this, this study will focus on the 1.5 and 2.0 mm cases only, each considering default settings of NRA (= 104).

The size of the computational domain was determined such to encompass the entire height of the flame in the positive z-direction, and to reduce possible effects of domain boundaries. An overview of the simulation setup is presented in Fig. 1, where the 1.5 mm case is shown for illustration. In the 1.5 mm case, the sample is 82.5 mm wide and 198 mm long; and the domain extends for 264 mm×148.5 mm×180 mm in the x-, y- and z-directions. In the 2.0 mm case, the sample is 102 mm wide and 192 mm long; and the domain extends for 256 mm×170 mm×150 mm in the x-, y- and z-directions.

The simulation domains were subdivided into multiple meshes to enable parallel computation. The most refined case, with 1.5 mm cells, was divided into 162 meshes, while the 2.0 mm cells were divided into 80 meshes. A high-performance computing cluster, consisting of 268 worker nodes with a total of 17 152 cores, was used to run the simulations. Each worker node features two AMD EPYC 7452 32-Core processors, each operating at a base clock speed of 2.350 GHz, and is equipped with 256 GB of memory, corresponding to 4 GB per core.

2.2. Analysis of small MLR peaks

In this study, the pyrolysis scheme from the original UMD Model is modified by introducing a small MLR peak to improve the fit of the model to experimental MLR data. This peak corresponds to a pyrolysis reaction consuming 0.5 % to 2 % of the initial mass of the sample, represented as reaction R3 in . The mass fraction decomposed by R3, named $PMMA_{imp}$, represents a portion of the virgin PMMA sample that may contribute to small MLR fluctuations. While $PMMA_{imp}$ does not represent a specific chemical component, it serves as a placeholder for minor impurities or alternative degradation pathways not captured by the reactions in the original model (R1 and R2).

The small peak will be described and analysed through the following three parameters:

- the peak temperature (T_p) of the small R3 peak;
- the pyrolysis range (ΔT) of the small R3 peak (i.e. peak width);

- the initial mass fraction (m_0) of $PMMA_{imp}$, associated with the small R3 peak.

Since all pyrolysis reactions of PMMA are assumed first-order, the order of reaction is fixed at $n = 1$ and its influence is not included in the analysis. Furthermore, as the focus lies on the kinetic parameters, the importance of the heat of reaction of R3 is also not evaluated in this study, and its value is fixed at $5.0\,kJ \cdot kg^{-1}$ as presented in Table 2.

In Fig. 3, red arrows highlight three key regions of the MLR curve where the introduction of a small peak could enhance the model's alignment with the experimental data. For instance, a small peak with a pyrolysis range of $\Delta T = 80\,°C$, decomposing 1 % of the initial mass of the material, can be placed at 210 °C, 284 °C or 420 °C, as shown in Fig. 4(a). The total resulting MLRs, presented in Fig. 4(b), which combine the UMD Model with the R3 peak at each location, show better agreement with the experimental data than the original UMD Model alone. This improvement in fit is reflected in Fig. 5, where the reduced root mean square error (RMSE) quantifies the enhanced match between each modified model and the experimental TGA data. However, multiple combinations of peak temperature, peak width, and mass fraction could define a small peak like R3 that enhances the fit of the model within these regions, allowing for further exploration of optimal parameters.

In this sense, another aspect of this study is to systematically examine the relationship between the simulation model and the introduced small peak, extending beyond the three main regions highlighted by the red arrows in Fig. 3. By varying the position of the small peak across the full temperature range associated with PMMA pyrolysis, the model's sensitivity to this peak is evaluated in a broader context. This is motivated by generalised approaches [10,11], where adding a third peak (R3) could improve the overall fit of the total MLR to the experimental data, not only in regions where distinct peaks are observed but also in areas where it might overlap with existing peaks in the model.

The primary aim of this study is to explore how variations in the parameters defining the small peak are reflected in the ROS predicted by the flame spread simulation. Specifically, we seek to determine whether certain regions of the MLR curve should be preferentially covered by the model, given that they may generate more significant changes in the ROS. Additionally, this study seeks to understand how the flame spread simulation responds to variability in the small peak's characteristics in a systematic manner, providing insights into the most relevant configurations for improving the pyrolysis model fidelity.

Two different methods were used to evaluate the effect of small MLR peaks on the ROS. In the first method, the parameters T_p, ΔT and m_0 were varied one-at-a-time to assess their individual impacts on the ROS, with results discussed relative to different simulation references. While this approach can highlight individual parameter effects, it does not fully capture how each parameter contributes to the overall variability of the ROS across its entire range of values. This is because it only measures responses to isolated changes rather than the cumulative impact of each parameter as it varies throughout the entire parameter space. This means that it may overlook how sensitive the ROS is to the full scope of possible variations in each parameter, providing only a partial assessment of their relative importance. To address this limitation, the second method combines an uncertainty analysis with a global sensitivity analysis, both performed using a polynomial chaos expansion (PCE) approach. These methods offer a more comprehensive view and are described in detail in the following sections.

2.2.1. One-at-a-time analysis

In this approach, the goal is to investigate the individual impacts of the parameters defining the small R3 peak (T_p, ΔT, m_0) on the ROS. Four groups of simulations were created, considering two mass fractions of $PMMA_{imp}$, $m_0 = 0.01$ and $m_0 = 0.02$; and two gas phase resolutions of 1.5 and 2.0 mm cells. The groups were labelled with two characters for easier reference: the first character denotes the $PMMA_{imp}$ mass fraction, and the second character denotes the cell size. A mass fraction of 0.01 is represented by "1", and 0.02 is represented by "2". Similarly, a cell size of 1.5 mm is represented by "a", and 2.0 mm is represented by "b". For example, "Group 2a" is composed by simulations where the mass fraction of $PMMA_{imp}$ is fixed at 0.02, and the gas phase cell size is 1.5 mm. Additionally, two simulation cases corresponding to the same cell sizes, where only the original UMD Model is used, were named Cases 0a and 0b. Table 3 presents a summary of the simulation groups and cases considered in the analysis.

For each group of simulations detailed in Table 3, the peak temperature T_p was varied one-at-a-time, while maintaining ΔT at constant 80 °C. Then, T_p was held fixed at 210 °C and ΔT was varied independently, but only in the coarser simulation cases, i.e. Groups 1b and 2b. This limitation aimed to save computing time, considering the expected lower impact of ΔT in comparison to T_p. The variation intervals for these parameters were established based on their initial values: $T_p = 210\,°C$ and $\Delta T = 80\,°C$ for the R3 peak, as well as on the observed variability in the total MLR from TGA data (see Fig. 3 and Table 2).

Starting from an initial peak temperature of $T_p = 210\,°C$, the variation interval for T_p was defined to range from 80 % to 200 % of 210 °C, resulting in a range of 168 to 420 °C. From the lower limit of this interval, temperature points for T_p were sampled at increments of 10.5 °C (5 % of 210 °C). This strategy produced 25 samples, each of which was used in a different flame spread simulation, with all other simulation settings kept fixed and unchanged within a group. The 25 different positions of peak R3 associated with the T_p samples are illustrated in Fig. 6. Overall, 100 simulations were conducted to study the effect of T_p across the four simulation groups.

Similarly, the variation interval for ΔT was defined to range from 80 % to 200 % of 80 °C, resulting in a range of 64 °C to 160 °C. From this interval, 25 samples were generated at increments of 4 °C, which corresponds to 5 % of 80 °C. The R3 peaks resulting from the ΔT samples are presented in Fig. 7, where the effect on the width of R3 can be clearly observed. As ΔT is varied within Groups 1b and 2b only, a total of 50 flame spread simulations were performed to analyse the effect of this parameter considering the current approach.

The effects of the parameters T_p and ΔT on the ROS of the flame spread simulations were assessed as percentage variations relative, to a reference ROS, as described by the following expression:

$$\text{Variation} = \frac{(\text{ROS}_{\text{param}} - \text{ROS}_{\text{ref}})}{\text{ROS}_{\text{ref}}} \times 100 \tag{4}$$

Here, $\text{ROS}_{\text{param}}$ denotes the ROS calculated from simulations with varied T_p and ΔT, while ROS_{ref} represents the ROS associated with the reference simulation case. The expression provided by Eq. (4) enables the evaluation of negative and positive changes in the ROS, depending on the position and the amplitude of the small R3 peak.

In the analysis, simulation Cases 0a and 0b were chosen as references to determine ROS_{ref}. This provides a suitable starting point, as these cases employ the original UMD Model without the R3 peak. To ensure consistency, only simulations with the same gas-phase cell size were compared against each other. Specifically, Case 0a was used as the reference for simulation Groups 1a and 2a, while Case 0b served as the reference for Groups 1b and 2b. This baseline comparison allows to quantify the overall influence of incorporating the R3 peak into the UMD Model, assessing how the inclusion of a small R3 peak affects the ROS relative to the original model.

2.2.2. Uncertainty quantification and global sensitivity analysis

The primary objective of this approach is two-fold. Firstly, it aims to quantify the uncertainty propagated to the ROS predicted by the 2 mm (gas phase resolution) simulation case due to the inclusion of the small peak in the pyrolysis model. Following the same line of reasoning as in the one-at-a-time analysis, the small peak is defined in terms of the parameters T_p, ΔT and m_0. In this part, the expected ROS value

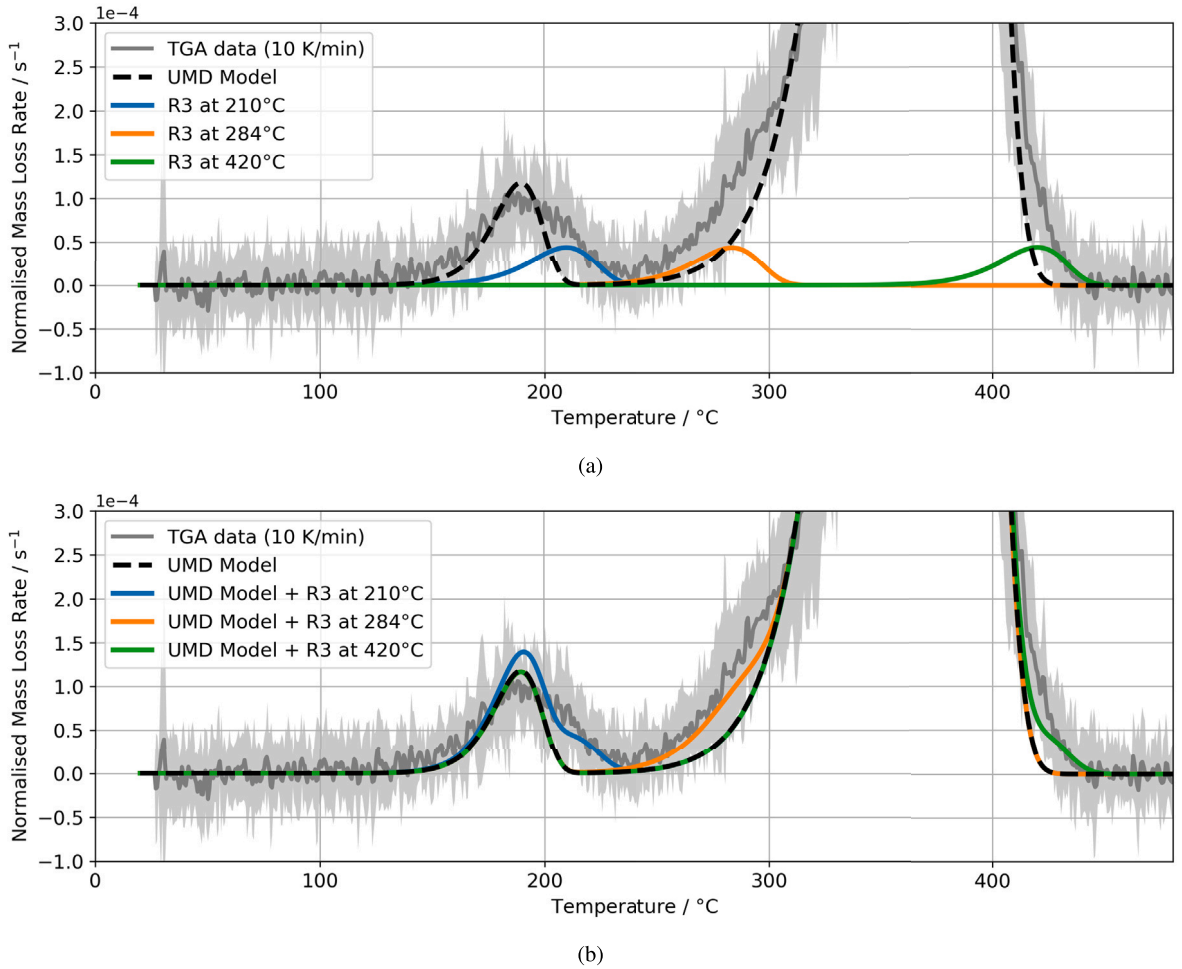

Fig. 4. Zoomed-in view of the normalised mass loss rate curves. Figure (a) shows possible locations for the small R3 peak, which can improve agreement with the experimental TGA data. Figure (b) displays the combined mass loss rate from the UMD Model and the R3 peak at each of these locations, illustrating the improved alignment with the experimental data [21] compared to the original UMD Model [7].

Table 3
Reference simulation cases and groups of simulations considered in the one-at-a-time approach.

Label	Material composition (PMMA sample)	Cell size (gas phase)	Pyrolysis reactions	Varying one-at-a-time
Group 1a	99 % $PMMA_{melt}$ + 1 % $PMMA_{imp}$	1.5 mm	(R1+R2+R3)	T_p
Group 1b	99 % $PMMA_{melt}$ + 1 % $PMMA_{imp}$	2.0 mm	(R1+R2+R3)	T_p, ΔT
Group 2a	98 % $PMMA_{melt}$ + 2 % $PMMA_{imp}$	1.5 mm	(R1+R2+R3)	T_p
Group 2b	98 % $PMMA_{melt}$ + 2 % $PMMA_{imp}$	2.0 mm	(R1+R2+R3)	T_p, ΔT
Case 0a	100 % $PMMA_{melt}$	1.5 mm	UMD Model (R1+R2)	–
Case 0b	100 % $PMMA_{melt}$	2.0 mm	UMD Model (R1+R2)	–

as well as its associated uncertainty are estimated. Secondly, it focuses on determining the contribution of each parameter defining the small peak to this uncertainty. To this end, a global sensitivity analysis is conducted, in which the influence of each parameter is quantitatively determined [37].

The uncertainty in the parameters defining the small peak was determined based on the variation intervals used in the one-at-a-time analysis. These intervals, referred to as uncertainty intervals, are summarised in Table 4. The methodology for determining the uncertainty in the peak temperature (T_p) and the pyrolysis range (ΔT) follows the same approach as in the previous analysis. However, the uncertainty in the mass fraction decomposed by the small peak is extended at its lower limit to account for even smaller peaks, which are considered to decompose between 0.5 % and 2 % of the total mass of the material. All input variables were assumed to be uniformly distributed within their respective intervals. The main goal is to understand how a given small peak, characterised by any combination of T_p, ΔT, and m_0 within these intervals of uncertainty, affects the predicted ROS.

Table 4
Intervals of uncertainty of the parameters associated with the small R3 peak.

Parameter	Intervals of uncertainty	Units
Peak temperature (T_p)	[168; 420]	°C
Pyrolysis range (ΔT)	[64; 160]	°C
Mass fraction (m_0)	[0.005; 0.02]	–

In this analysis, a non-intrusive polynomial chaos expansion (PCE) method was adopted. PCEs are polynomial approximation techniques specifically designed for facilitating uncertainty quantification and sensitivity analysis. By treating the model as a "black box", the PCE approach approximates the model using only its input–output data. It treats the uncertain model inputs as random variables and represents

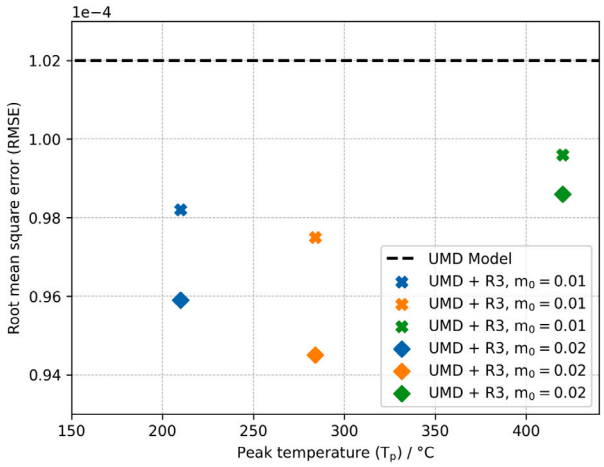

Fig. 5. RMSE of the different pyrolysis models compared to the average experimental TGA data. The modified models incorporate the R3 peak with mass fractions of $m_0 = 0.01$ and $m_0 = 0.02$, at three main temperatures: 210 °C, 284 °C, and 420 °C. The inclusion of the R3 peak at these temperatures in the UMD Model [7] generally reduces the RMSE, indicating improved agreement with experimental data [21].

the model as orthogonal polynomials of these inputs. This provides a cost-effective framework compared to techniques based on Monte Carlo estimates, which require a very large and often prohibitive number of simulation runs to determine statistical properties accurately [31,38]. The analysis described in this section was carried out using the Python library `chaospy` [4].

The flame spread simulation is represented by a function f that provides the output of interest Y; f varies in space $\boldsymbol{x}$ and time t, and depends on a vector of input parameters $\boldsymbol{Q} = (Q_1, Q_2, \ldots, Q_d)$, as expressed in the following equation:

$$Y = f(\boldsymbol{x}, t, \boldsymbol{Q}) \tag{5}$$

Here, the model output of interest is the ROS, and the uncertain parameters are those describing the small peak, as defined earlier: T_p, ΔT, and m_0. A general polynomial approximation for f can be defined as:

$$f \approx \hat{f}(\boldsymbol{x}, t, \boldsymbol{Q}) = \sum_{n \in I_N} c_n(\boldsymbol{x}, t)\boldsymbol{\Phi}_n(\boldsymbol{Q}), \quad I_N = \{0, \ldots, N\} \tag{6}$$

where n ranges over I_N and N represents the highest order of the polynomials used in the expansion. The term $c_n(\boldsymbol{x}, t)$ denotes the coefficients of the expansion, and $\boldsymbol{\Phi}_n(\boldsymbol{Q})$ represents the polynomials in the expansion. The PCE is constructed so that the polynomials are orthogonal to the joint probability density function of the uncertain inputs. The three-term recurrence relation is used to compute the PCE [4].

The coefficients of the expansion $c_n(\boldsymbol{x}, t)$, also known as the Fourier coefficients, can be estimated using various methodologies, including intrusive and non-intrusive approaches [4]. Recently, Jamil and Brännström [39] compared the performance of both intrusive and non-intrusive methods for quantifying uncertainties in pyrolysis models based on PCE. They concluded that the non-intrusive projection method led to faster convergence than the point collocation method, particularly when dealing with a limited number of uncertain inputs. Given these findings and the complexity of the flame spread simulation model, which makes intrusive methods impractical, the projection method was chosen for this work.

The projection method approximates the coefficients of the polynomial expansion using a numerical integration scheme. Here, Gaussian quadrature was employed, which requires the function to be evaluated at specific points, known as quadrature points, that correspond to samples of the input parameters. The number of samples is determined by the order of the polynomial expansion N and the number of uncertain input parameters d, as defined by: $(N+1)^d$. The PCE order is chosen to match the order used in the quadrature rule.

In this study, two PCEs were developed for orders 2 and 3. The quality of these approximations was evaluated based on a global RMSE, using input–output data from the one-at-a-time analysis of Groups 1b and 2b. The best PCE approximation is determined based on the lowest value of global RMSE. For each order, the number of samples (and consequently the number of simulation runs) was 27 for the second-order PCE and 64 for the third-order PCE, given that the number of uncertain parameters describing the small peak is 3. The uncertainty in the ROS induced by these uncertain parameters is expressed in terms of the standard deviation.

The influence of each parameter is expressed quantitatively through the Sobol sensitivity indices [3]. The method is based on the decomposition of variances, where the total variance of the output of the model is split into partial variances attributed to individual input parameters, as well as their interactions. The indices are obtained by dividing each partial variance by the total variance of the output, providing ratios from 0 to 1. For example, given an input vector $\boldsymbol{Q} = (A, B, C)$, the indices become:

$$S1_A + S1_B + S1_C + S2_{AB} + S2_{AC} + S2_{BC} + S3_{ABC} = 1 \tag{7}$$

where $S1_A$, $S1_B$, and $S1_C$ are the first-order indices, accounting for the main effects of A, B, and C respectively. The second-order indices $S2_{AB}$, $S2_{AC}$ and $S2_{BC}$ account for the interaction effects between the pairs of inputs in their subscripts. Accordingly, $S3_{ABC}$ is the third-order index which accounts for the interaction effects on the output when A, B and C are varied together.

The indices provide a measure of the contribution of each input parameter to the overall output variance. Specifically, the first-order indices (S1) represent the independent effect of each parameter, indicating the portion of output variance that can be attributed directly to variations in that parameter across its entire range of values. Unlike the one-at-a-time analysis, which examines individual effects by varying one parameter at a time, the S1 indices offer a more comprehensive assessment by capturing each parameter's influence on output variability across the entire parameter space.

The higher-order indices (S2, S3, etc.) capture the combined influence of the parameters in their subscripts on the output variance. The total-order sensitivity indices (ST) account for both main and interaction effects, representing the overall contribution of a parameter to the output variance [40]. For example, the ST index of parameter A is given by $ST_A = S1_A + S2_{AB} + S2_{AC} + S3_{ACB}$ [31,40]. When interaction effects exist in the model, the sum of all ST indices (e.g., $ST_A + ST_B + ST_C$) is greater than 1.

3. Results and discussion

3.1. One-at-a-time analysis

3.1.1. Qualitative effects on the HRR and flame position curves

The qualitative effects of one-at-a-time variations in the peak temperature T_p, pyrolysis range ΔT and mass fraction m_0 are initially discussed for simulations in Group 2b. This group is particularly selected because it showed the largest responses to changes in all input variables defining the R3 peak. This effect is attributed to the larger amount of material decomposed by the small peak in Group 2b, where it accounts for 2 % of the total material mass, compared to 1 % in Groups 1a and 1b. The effects related to the mass fraction decomposed by the small peak will be further discussed in the next section.

The peak temperature T_p had a significantly larger influence on the HRR and flame position curves than the pyrolysis range ΔT. This difference is illustrated by the discrepancy in the HRR curves, as shown in Figs. 8 and 9 for simulations in Group 2b. The plots show greater variability in the HRR when T_p was varied (Figs. 8(a) and 9(a))

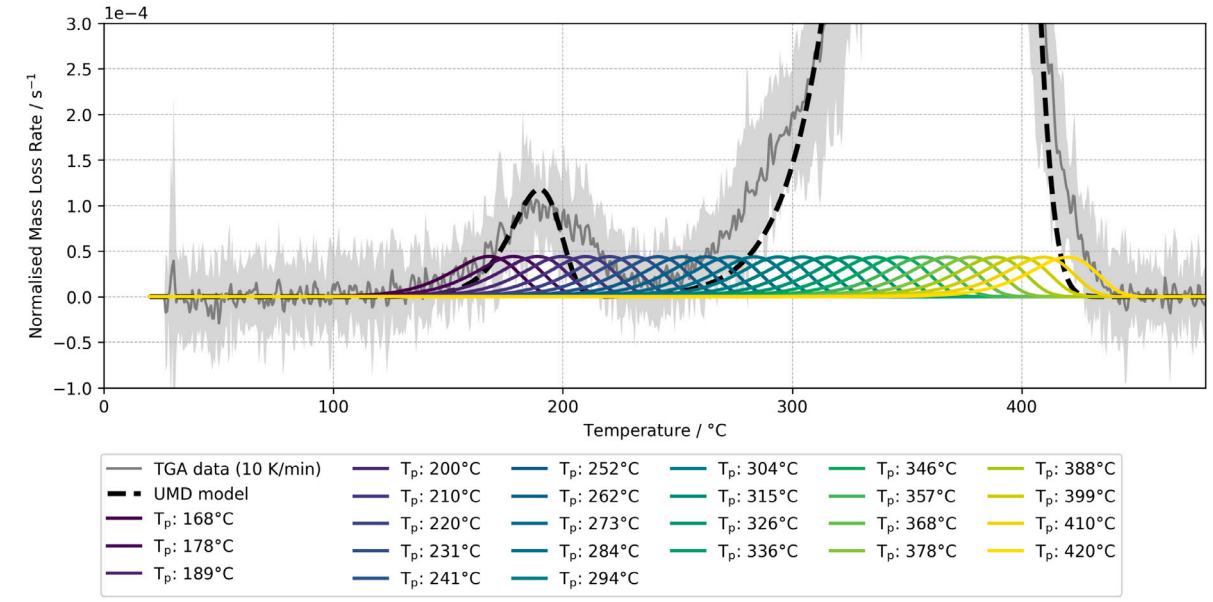

Fig. 6. Variation of the R3 peak position by adjusting the peak temperature (T_p) incrementally between 168 °C and 420 °C. Each position creates a distinct pyrolysis model, used in the flame spread simulation to evaluate the impact of R3 position on the ROS.

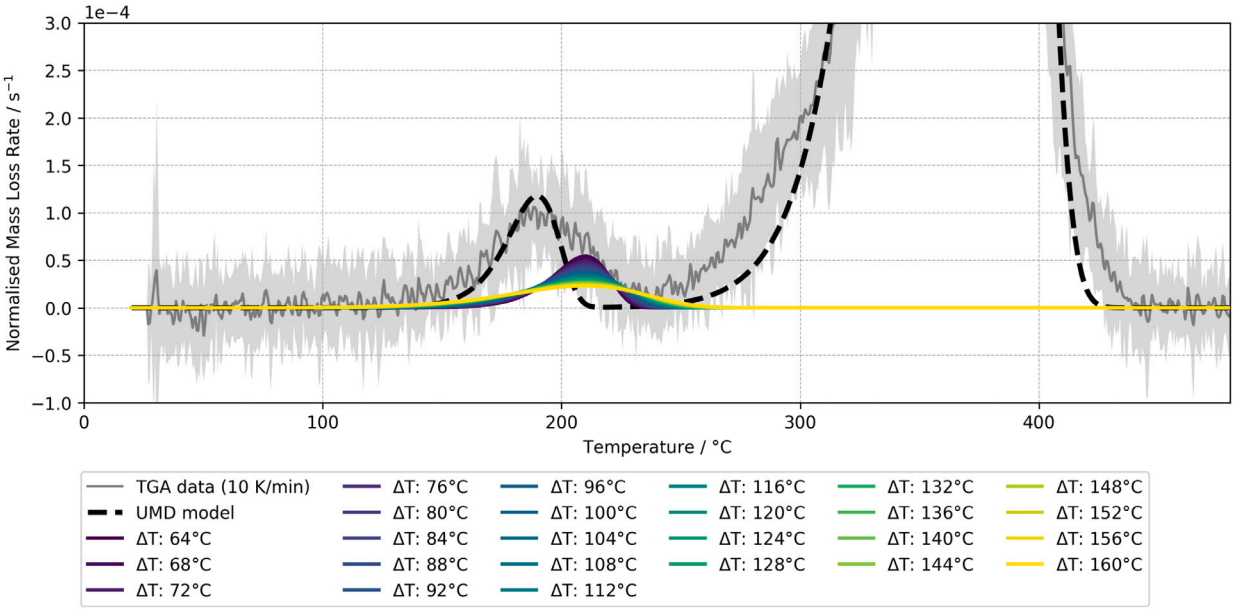

Fig. 7. Variation of the R3 pyrolysis range (ΔT), shifted one-at-a-time between 64 °C and 160 °C. Each ΔT value results in a different pyrolysis model, used in the flame spread simulation to evaluate the impact of R3 width on the ROS.

compared to when ΔT was varied (Figs. 8(b) and 9(b)). In Figs. 8 and 9, the curves are colour-coded to represent respectively the specific values of T_p and ΔT used in each simulation, following the colour pattern presented previously in Figs. 6 and 7. Additionally, it is important to bear in mind that when T_p is varied one-at-a-time, ΔT is fixed at 80 °C and when ΔT is varied, T_p is fixed at 210 °C.

Fig. 8(a) clearly demonstrates the reversal effect of increasing T_p on the HRR: as T_p is moved from lower to higher values, the HRR decreases, particularly during the self-sustained spread phase. When the peak temperature T_p is set to higher values (see Fig. 6), the material associated with the R3 peak begins to decompose only at these elevated temperatures, which reduces the available combustible mass at lower temperatures. This delayed decomposition leads to a lower HRR, as shown in Fig. 8(a).

In turn, this reduction in the HRR yields lowered heat flux reaching the sample surface, slowing down the heating-up process of the material and decreasing the pyrolysis rates. Consequently, the flame advances more slowly over the unburnt material. This tendency is reflected in flattened slopes of the flame position curves, which is more clearly visible in Fig. 9(a). From an inverse viewpoint, Fig. 8(a) also illustrates the opposite effect of decreasing T_p on the HRR. As T_p decreases from higher to lower temperatures, the material starts to pyrolyse earlier, releasing more mass for combustion at these temperatures, consequently leading to earlier sample consumption and increased HRRs.

Similarly, higher values of the pyrolysis range ΔT lead to a decrease in the HRR (Fig. 8(b)) and in the slope of the flame position curves (Fig. 9(b)). Initially, it was expected that wider peaks would directly increase the HRR because the rates at the peak tails are also increased.

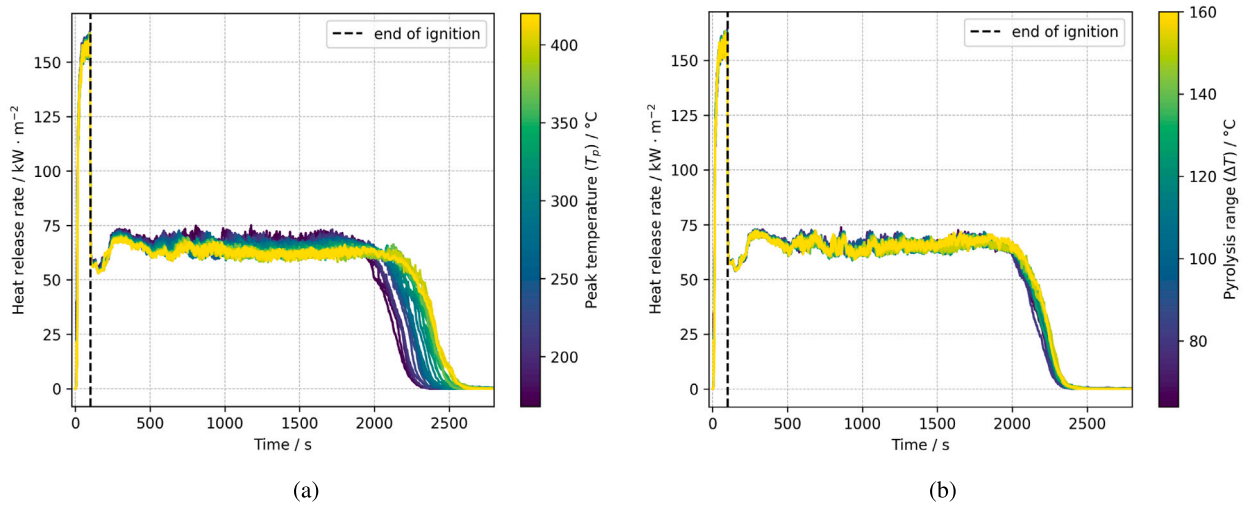

Fig. 8. Qualitative effects on the HRR induced by changes in the (a) peak temperature (T_p) and (b) pyrolysis range (ΔT) of the small peak in simulations from Group 2b.

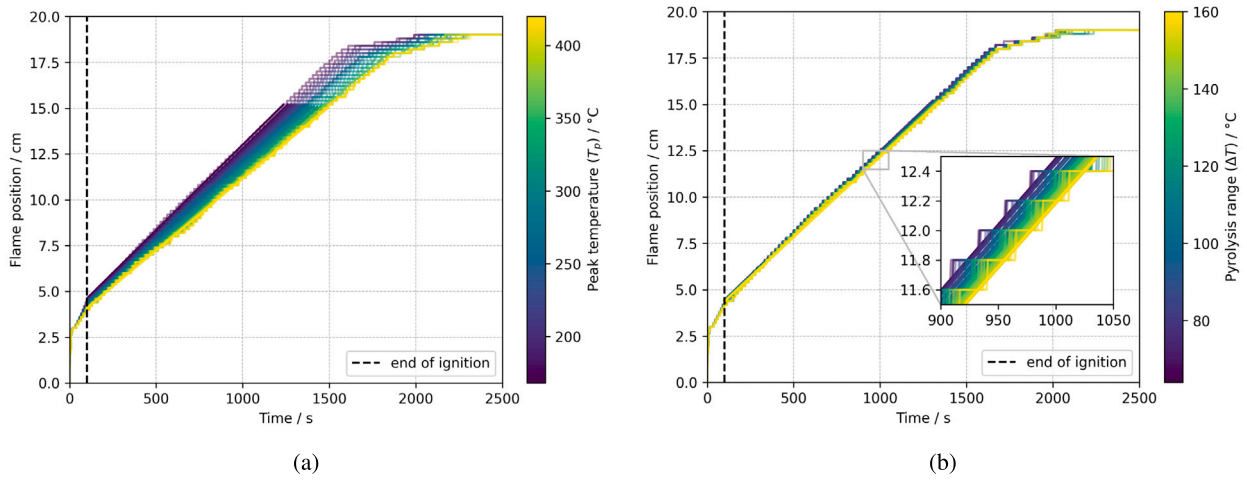

Fig. 9. Qualitative effects on the flame position curves induced by changes in the (a) peak temperature T_p and (b) pyrolysis range ΔT of the small peak in simulations from Group 2b.

However, there is a competing effect: as the width of the peak increases, the rates around the peak's maximum values are diminished, as shown in Fig. 7. This effect is dominant because more mass is decomposed at these lower rates. Consequently, the net effect of larger ΔT values is a slower overall pyrolysis and heat release rates.

The qualitative analysis suggests that both changes in T_p and ΔT show a similar general effect: larger values of T_p and ΔT produce an inverse effect on the HRR and on the slope of the flame position curves shown in Fig. 9. However, the impact of ΔT is practically negligible compared to the influence of T_p. For this reason, from this point forward in the text the results and discussions will focus on the effects of T_p and m_0, across all simulation groups described in Table 3.

3.1.2. Effects on the rate of spread (ROS)

Within the self-sustained phase of each simulation case, the relationship between the flame position and time was approximated using a linear function, as presented in Figs. 9(a) and 9(b). The first derivative of this linear function represents the rate of change of the flame position (specifically, the leading edge) with respect to time, here referred to as the ROS.

The ROS values for each simulation within each group are plotted against the corresponding T_p values used in each simulation, as depicted in Fig. 10(a). In this plot, the two gas phase grid resolutions used are denoted by different markers: triangles indicate the 1.5 mm resolution, while circles refer to the 2.0 mm resolution. The solid markers highlight the positions of the R3 peak at 210 °C, 284 °C and 420 °C, which are key positions in the MLR temperature range as indicated before in Fig. 4. The ROS values for the reference simulation cases (Case 0a and 0b) that employed the original UMD Model are also presented. Since in the reference cases a small peak like R3 is not present, it is not meaningful to establish a relation between the ROS and the parameters describing the small peak. Therefore, the ROS values for these cases are represented as horizontal lines in the figures, serving as a baseline for comparison.

The trends observed in Fig. 10 indicate that the ROS decreases more rapidly at lower T_p values, with the rate of decrease slowing as T_p continues to rise. This suggests that at more elevated temperatures, the ROS values converge towards those of reference Cases 0a and 0b, becoming nearly identical at $T_p = 420$ °C. Specifically, Groups 1a and 2a, which have the same gas phase cell size, align with Case 0a, while Groups 1b and 2b align with Case 0b. Understanding this behaviour is crucial for assessing the impact of incorporating a small peak like R3 into the pyrolysis model. This behaviour highlights that the effect on the ROS is more pronounced when the small peak is positioned at lower temperatures and practically negligible when it is located at higher temperatures.

Moreover, Groups 2a and 2b start with higher ROS values and show a steeper decline compared to Groups 1a and 1b. This observation suggests a stronger sensitivity of Groups 2a and 2b to T_p changes, indicating that the simulations in these groups are more affected by T_p than those in Groups 1a and 1b. This increased sensitivity comes from the larger mass fraction decomposed by the small peak in simulations from Groups 2a and 2b (2 % $PMMA_{imp}$, $m_0 = 0.02$), as opposed to simulations in Groups 1a and 1b (1 % $PMMA_{imp}$, $m_0 = 0.01$). When T_p is reduced, a greater amount of material in Groups 2a and 2b undergoes pyrolysis at these lower temperatures. With this, more combustible gas is released earlier from a burning surface cell, leading to a larger flame. The flame in turn releases more heat and heats up surrounding, not yet burning, surface cells faster. Consequently, this feedback loop leads to an increased HRR and sustains the flame spread. In this sense, the larger initial mass fraction in Groups 2a and 2b results in a more pronounced effect of T_p changes on the ROS, leading to the observed steeper decline in ROS as the material decomposes more rapidly at lower temperatures. This dynamic highlights the critical role of m_0 and T_p in determining the ROS sensitivity to the inclusion of the small R3 peak in the original model.

The effects induced by changes in the position of the small peak, through variations in T_p, are more clearly illustrated through the percentage variation in the ROS, as shown in Fig. 10(b). The ROS of Case 0a is used as the reference for Groups 1a and 2a, while Case 0b serves as the reference for Groups 1b and 2b. The grey-shaded area in Fig. 10(b) represents a 5 % variation around the reference cases (0a and 0b), which is highlighted here as it is considered indicative of low variation.

The plot in Fig. 10(b) shows that percentage variations in ROS consistently exceed the 5 % threshold across all simulation groups as T_p decreases. In Groups 2a and 2b, this threshold is surpassed when R3 is positioned within the temperature range of approximately 168 °C to 310 °C. For Group 1a, the ROS exceeds this threshold when R3 is located between 168 °C to 210 °C, while in Group 1b, the threshold is surpassed for R3 placements within 168 °C to 240 °C. The largest ROS increase observed is over 18 % for peaks with a mass fraction of 0.02 and 10 % for peaks with a mass fraction of 0.01, occurring when $T_p = 168$ °C. These maximal ROS variations, ranging from 10 % to 18 %, represent the theoretical upper limits of the ROS's sensitivity to the addition of the small R3 peak at 168 °C. Along with the intermediate variations observed as the R3 peak is shifted across the pyrolysis temperature range, these results provide insight into the extent to which the predicted ROS responds to this adjustment in the original model.

Particular attention should be paid to the solid markers in Fig. 10, which identify specific cases where the R3 peak is positioned at 210 °C, 284 °C, and 420 °C (as shown in Figs. 3 and 4(a)). These peak positions are especially significant as they improve the alignment between the model and the experimental TGA data by refining the fit at the shoulders of the main peaks in the original model. Among these configurations, the largest ROS variations occur when the R3 peak is positioned at 210 °C. This placement leads to an approximate ROS increase of 13 % for a mass fraction of 0.02 and 6 % for a mass fraction of 0.01, as shown by the solid markers in Fig. 10(b). Note, that the R3 peak with a mass fraction of 0.02 positioned at 210 °C, leads to a better representation of the sample pyrolysis as indicated by the reduced RMSE (Fig. 5).

In the context of the present theoretical study, these variations are considered to represent a significant influence on the ROS when the R3 peak is placed at 210 °C, particularly given that they result from the inclusion of small peaks decomposing only 1 % to 2 % of the material's total mass. However, in practical applications, the acceptability of such variability in the ROS depends on the specific context, and the degree of variability regarded as tolerable for a given application. This judgment should be informed by comparisons with experimental data and, most importantly, the associated experimental uncertainties. Typically, the predicted ROS should be evaluated relative to an experimentally averaged ROS and its uncertainty range to determine whether the observed variability falls within acceptable limits.

As illustrated in Fig. 5, the fit to experimental TGA data improves relative to the original model across all tested R3 peak locations marked by solid markers in Fig. 10(b), with the best alignment achieved when R3 is placed at 284 °C. However, for a fixed mass fraction, this position – while yielding the lowest RMSE compared to the TGA data – does not correspond to the largest ROS variations. This result indicates a distinction between optimising model fit to TGA data and the ROS sensitivity to the inclusion of the small R3 peak. While positioning the R3 peak at 284 °C provides the most accurate reproduction of the experimental MLR data, its impact on ROS is relatively moderate compared to 210 °C. This suggests that improving the fit to TGA data does not always translate to equivalent changes in ROS predictions. More importantly, these findings highlight which specific deviations between the original model and experimental data, as shown in Fig. 3, should be given greater attention when refining the model fit: deviations in low-temperature regions, should be prioritised over adjustments in high-temperature regions. This is because the ROS is more sensitive to peaks positioned in the lower-temperature range, making them more influential on ROS predictions.

The plots in Fig. 10 demonstrate that the non-linear decay in the ROS as T_p is increased is consistent across the different simulation groups. However, this decay is not smooth, as small oscillations are observed in the ROS for each simulation case. These oscillations are attributed to numerical artefacts, primarily due to default settings in FDS that impact the temporal and spatial resolutions of the radiation field. By default, these settings result in the radiation transport equation being fully updated only every 15 time steps. This update frequency may lead to delays in radiation transport across the domain, especially when multiple meshes are used [32]. While a detailed investigation into these effects is beyond the scope of this study, preliminary tests (not shown) suggest that the impact of these artefacts on the results is negligible. Addressing the issue by increasing the update frequency of the radiation field would significantly increase computational demands, rendering such adjustments impractical for the purposes of this work.

Another important factor affecting the ROS predictions shown in Fig. 10(a) is the gas-phase cell size. In both simulation groups, the higher-resolution cases (Group 1a and Group 2a) predict larger ROS values than their lower-resolution counterparts (Group 1b and Group 2b). In this setup, the 'a' denotes higher resolution, which leads to these increased ROS predictions (see Table 3). Higher mesh resolutions enhance the spatial accuracy of heat transfer calculations, resulting in increased heat fluxes reaching the sample, which in turn raises the predicted ROS. However, while finer resolutions theoretically enhance the predictive accuracy of the model, validation against experimental data is essential to confirm any actual improvements. Further validation is also needed to determine how the ROS variations observed in this study translate into meaningful improvements in model predictions.

With respect to validation of the ROS against experimental data: as of writing this article, no comparable small-scale flame spread experiment data with the MaCFP PMMA is available. Qualitatively, a comparison with work by Korobeinichev et al. [41] can be made. They performed flame spread experiments over horizontal on cast PMMA of the same width (100 mm) under open-air conditions, placed on top of insulating material. However, the sample had a lower thickness of 5 mm than the 6 mm used by Fiola et al. [7]. Korobeinichev et al. reported a ROS of 6.0 mm min^{-1} [41]. The baseline simulation cases presented here (original UMD Model), predicted flame spread rates of 5.10 mm min^{-1} and 4.73 mm min^{-1} for gas-phase resolutions of 1.5 mm and 2.0 mm, respectively. It is expected that a thinner sample leads to a faster spread rate [41,42], thus the predicted ROS in this study seems reasonable. Considering this, along with the absence of reported experimental uncertainties, which limits further comparisons, the simulation models used in the present study are viewed as an adequate

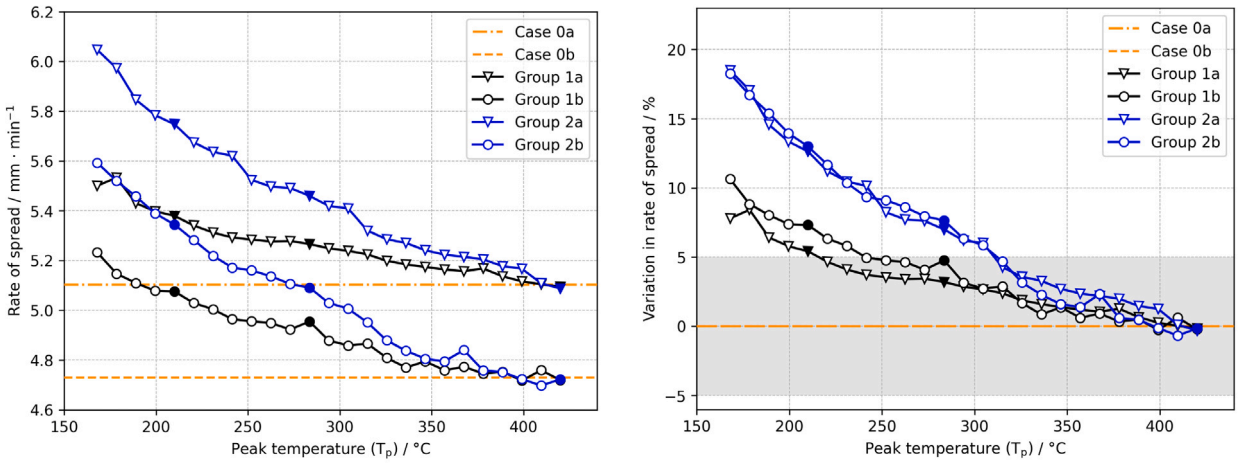

(a) (b)

Fig. 10. Effects on the rates of spread induced by changes in the peak temperature (T_p) of the small R3 peak. Results in black refer to peak mass fractions equals to $m_0 = 0.01$, and blue results refer to peak mass fractions equal to $m_0 = 0.02$. (a) Absolute values of ROS and (b) percentage variations in the ROS relative to the reference simulation Cases 0a and 0b. Solid markers highlight the positions of the R3 peak at 210 °C, 284 °C and 420 °C.

representation of the expected spread rates, even though they are not directly comparable. The selected sub-models represent state-of-the-art practices within FDS for predicting flame spread. As such, the results presented here draw attention to the relevance to the ROS predictions of accounting for small MLR peaks in the pyrolysis model, particularly those occurring at lower temperatures.

It is essential to point out that the ROS variations induced by the inclusion of the small R3 peak in the original UMD model are representative of the behaviour of the models and simulation setups considered in this study. Such models refer to the UMD Model as well as the selected sub-models and parameters within FDS that govern the simulation. The scope of this work is limited to examining how the ROS predicted for a horizontal flame spread over a PMMA plate responds to the inclusion of a small R3 peak when using the UMD model. It does not suggest that every predictive simulation model built with FDS would exhibit the same response to such modifications. That being said, it stands to reason that changes in the geometry of the combustible surfaces and their surroundings that would lead to faster flame spread for the UMD model, should qualitatively yield a similar response for the modified UMD models.

3.2. PCE-based analysis

To determine which of the chosen PCE orders best represents the general model behaviour, both second- and third-order PCEs were tested against the samples used in the one-at-a-time analysis. Specifically, input samples of T_p and ΔT from simulation Groups 1b and 2b were supplied to the PCE approximations to predict the ROS. It is important to note that such datasets were used solely for testing, and not for training the PCEs. The results for PCE orders 2 and 3 are shown in Fig. 11, where the solid circles represent the PCE predictions of the ROS, and the white circles the actual FDS predictions.

From Fig. 11 it can be seen that both PCE orders were able to capture the overall trend of the relationships between the ROS and the input parameters describing the small peak. As previously discussed, the fluctuations present in the FDS data are assumed to be artefacts related to the spatial resolution in the simulations. Therefore, not capturing these fluctuations in detail is not considered problematic. Instead, the focus is on capturing the general trends exhibited by the actual simulation data.

The proximity of PCE predictions and FDS predictions is measured by the RMSE. The RMSE results for each case presented in Fig. 11 are presented in Table 5. It can be observed that for datasets in Group 1b, the lowest RMSEs correspond to PCE order 2, whereas for datasets in Group 2b, the lowest RMSEs correspond to PCE order 3. These results indicate that the relationship between the ROS and the one-at-a-time variations in T_p and ΔT is better represented by the second-order PCE when the peak consumes 1 % of the total material mass, and by the third-order PCE when the peak consumes 2 % of the mass. This occurs because the second-order PCE is sufficient to capture the lower level of non-linearity observed for simulations in Group 1b. Similarly, the third-order PCEs can better capture increased non-linearities, which are more characteristic of the simulations in Group 2b.

Table 5
Root mean square errors (RMSE) calculated for each test dataset.

	Ref data	RMSE Group 1b	RMSE Group 2b	Mean RMSE
PCE order 2	Fig. 11(a)	0.024	0.041	0.033
	Fig. 11(b)	0.019	0.031	0.025
PCE order 3	Fig. 11(a)	0.027	0.036	0.031
	Fig. 11(b)	0.028	0.019	0.023

The results obtained from the PCE analysis for orders 2 and 3 are presented in Table 6. Both PCE orders lead to similar estimations of mean and standard deviation: the mean ROS converges to 4.9 mm min^{-1}, and the standard deviation converges to 0.2 mm min^{-1}. The mean ROS represents the overall expected ROS, taking into account the uncertainty in all three inputs T_p, ΔT and m_0, while the standard deviation represents the variability around this mean value, representing the uncertainty in the ROS. In terms of relative values, this result corresponds to ±8 % (two standard deviations) of variability in the ROS, induced solely by the uncertain parameters defining the small R3 peak.

Despite the consistent mean and standard deviation values obtained from both PCE orders, the sensitivity indices calculated from the second- and third-order PCE approximations show some non-negligible variability. As seen in Table 6, these differences are more significant for S1 and ST indices associated with parameters T_p and m_0. These differences can be attributed to the improved ability of higher-order polynomials to capture non-linearities. Since the sensitivity indices are calculated from the coefficients of the PCE, the inclusion of higher-order terms changes these coefficients and their interpretation. Consequently, the calculated sensitivity indices can vary, even though the mean and standard deviation might not significantly change, as the overall distribution shape is well captured by the lower-order terms.

For instance, with the PCE order 2, the S1(T_p) is equal to 0.76, indicating that 76 % of the uncertainty in the ROS stems from varying

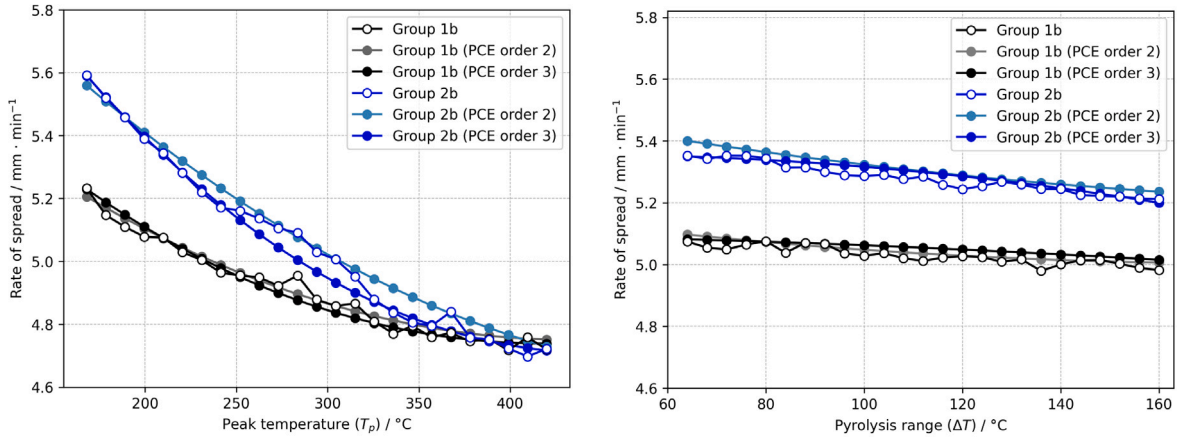

Fig. 11. Validation of PCE orders 2 and 3 against simulation data used in the one-at-a-time analysis.

Table 6
Uncertainty quantification and Sobol sensitivity indices.

	PCE order 2	PCE order 3
Mean ROS (mm min^{-1})	4.938	4.931
Standard deviation (mm min^{-1})	0.219	0.224
S1 (T_p)	0.76	0.81
S1 (ΔT)	0.02	0.01
S1 (m_0)	0.12	0.09
S2 (T_p, ΔT)	0	0
S2 (T_p, m_0)	0.09	0.08
S2 (ΔT, m_0)	0	0
S3 (T_p, ΔT, m_0)	0.01	0.01
ST (T_p)	0.85	0.90
ST (ΔT)	0.03	0.01
ST (m_0)	0.22	0.18

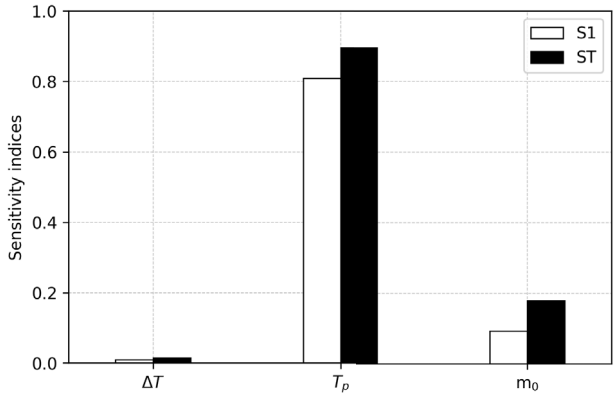

Fig. 12. First-order (S1) and total-order (ST) sensitivity indices for the parameters defining the small peak, estimated using the third-order PCE. The indices demonstrate that the peak position (T_p) is the dominant factor influencing the ROS, while the peak mass fraction (m_0) has a secondary effect, and the peak width (ΔT) plays a negligible role.

the position of the small peak (T_p) individually. In contrast, the PCE order 3 estimates this value to be 0.81 (81 %). In both PCE approximations, the estimations of the S2(T_p, m_0) indices are similar, showing that around 8 % to 9 % of the ROS uncertainty is caused by interaction effects between the peak position and the mass fraction of the small peak (m_0). Similarly, the S3 index, which indicates the interaction effects when all three inputs (T_p, ΔT, and m_0) are varied together, also does not change significantly between the PCE orders. Therefore, the variations observed in the ST indices between PCE orders mainly reflect the variation in the S1 indices.

Although the estimates of the ST indices vary between PCE orders, the overall ranking of parameter importance remains similar in both polynomial approximations. The consistently large values of ST(T_p) highlight the dominant role of the peak position (T_p) in the ROS uncertainty. To a considerably smaller extent, the peak mass fraction (m_0) is the second most important factor, followed by the minor role of the peak width (ΔT). This order of parameter importance aligns with the findings of the one-at-a-time analysis, which also demonstrated that the influence of the small peak on the ROS was primarily governed by T_p. It is worth pointing out that the indices capture the influence of the parameters not only at the specific samples used in the one-at-a-time analysis, but across the entire parameter space defined by the uncertainty intervals of each parameter. They therefore provide a global measure of parameter importance that extends beyond the limited scope of discrete sampling points.

To better illustrate how the parameters defining the small peak influences the ROS, the sensitivity indices in Table 6 estimated based on the third-order PCE are shown in a bar plot in Fig. 12. The plot highlights the dominance of the peak temperature T_p, with both first-order (S1) and total-order (ST) indices being significantly higher than those of m_0 or ΔT. While m_0 exhibits limited sensitivity, ΔT has negligible impact, consistent with the trends discussed above.

Fig. 13 shows the response surface that illustrates the relationship between the variation in the ROS and the two most influential parameters of the small peak, T_p and m_0. The ROSs were obtained from the third-order PCE approximation and variations were calculated relative to the ROS of Case 0b. The colour scale in the figures highlights key regions of the parameter space, visually depicting how combinations of T_p and m_0 influence the ROS. For instance, areas where the peak temperature T_p is low and the initial mass fraction m_0 is high correspond to the highest ROS variations, represented by light green and yellow hues, whereas the opposite effect is shown in dark blue shades. Additionally, the response surface includes combinations of T_p and m_0 used in the one-at-a-time analysis. Cases where m_0 was fixed at 0.01 and T_p was varied to 210 °C, 284 °C, and 420 °C are marked with diamond symbols, while cases where m_0 was fixed at 0.02 and T_p was varied similarly are indicated by crosses.

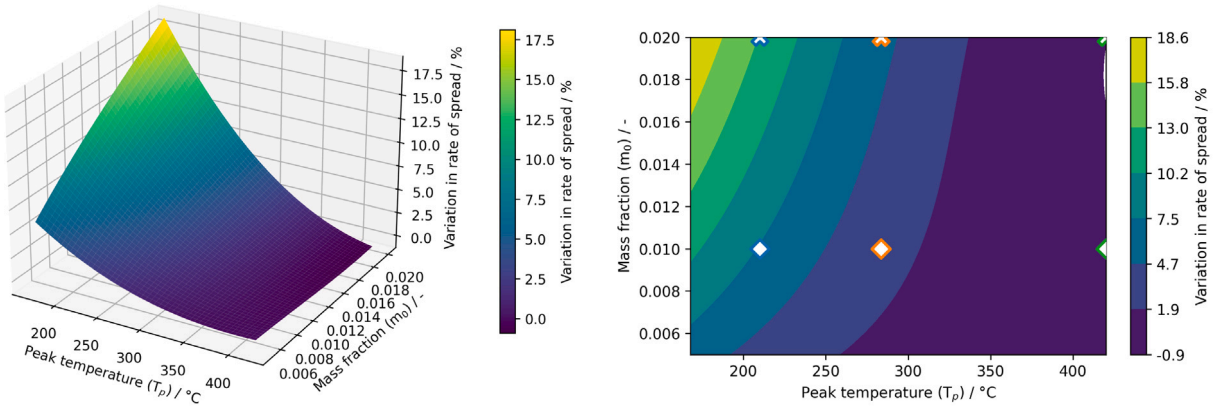

Fig. 13. Response surface illustrating the relationship between the variation in the ROS and the two most influential parameters of the small peak, T_p and m_0. The ROSs were obtained from the third-order PCE approximation and variations were calculated relative to the ROS of Case 0b. (a) 3-D view; (b) 2-D view, where markers indicate the combinations between T_p and m_0 used in the one-at-a-time analysis.

4. Conclusions

This study explored the impact of including an additional small MLR peak on the ROS predictions of a simplified flame spread simulation (horizontal flame spread over a PMMA sample) conducted using FDS. The peak was introduced to (i) improve agreement between the original pyrolysis model and measured TGA data, and (ii) to systematically investigate small MLR fluctuations occurring at various points along the pyrolysis temperature range. This study showed that the general approach of neglecting MLR fluctuations in modelling pyrolysis may not necessarily be valid, as there is at least one scenario where a non-negligible effect on the ROS can be demonstrated. Future work is needed to gain more understanding of this effect in general.

One-at-a-time and global sensitivity analyses were conducted, revealing that the peak position has the greatest impact on the ROS, followed by the peak mass fraction, while the peak width has a negligible effect. Specifically, it was demonstrated that the inclusion of a small peak can significantly influence the ROS predictions when the peak is positioned at lower temperatures, but has little to no effect when located at higher temperatures. This effect becomes more pronounced for peaks decomposing larger mass fractions, with ROS increases observed between 6 % to 13 % relative to the original model, for peaks decomposing 1 % to 2 % of the sample's total mass, respectively.

Within the scope of this theoretical study, these variations reflect the global behaviour of the simulation model, which incorporates submodels that represent state-of-the-art practices for predicting flame spread. Accordingly, the results obtained help understand the importance of improving the agreement between pyrolysis models and TGA data by accounting for small MLR fluctuations: while fluctuations at higher temperatures have a minor influence on the ROS and can be neglected, those at lower temperatures can significantly enhance the predicted spread rates and should not be overlooked. Yet, in practical applications, whether or not such variabilities in the ROS are acceptable, depends on the specific context and the degree of variation considered tolerable for a given scenario. Ideally, this judgment should be informed by comparisons with averaged experimental data and, most importantly, the associated experimental uncertainties.

Finally, this first step towards understanding the role of minor pyrolysis reactions may support the question about the impact of experimental variations in TGA measurements. A general quantification of the impact of MLR fluctuations may define the accuracy and precision needed from TGA measurements.

Acronyms

FDS	Fire Dynamics Simulator
HRR	Heat release rate
MCC	Microscale combustion calorimeter
MLR	Mass loss rate
PCE	Polynomial Chaos Expansion
PMMA	Poly(methyl methacrylate)
$PMMA_{melt}$	Material component of PMMA sample
$PMMA_{int}$	Intermediate component from $PMMA_{melt}$ pyrolysis
$PMMA_{imp}$	Material component of PMMA sample
$PMMA_{gas}$	Combustible gas from PMMA pyrolysis
RMSE	Root mean square error
ROS	Rate of spread
R1	Pyrolysis reaction associated with $PMMA_{melt}$
R2	Pyrolysis reaction associated with $PMMA_{int}$
R3	Pyrolysis reaction associated with $PMMA_{imp}$
S1	First-order sensitivity index
S2	Second-order sensitivity index
S3	Third-order sensitivity index
ST	Total-order sensitivity index
TGA	Thermogravimetric analysis
T_p	Peak temperature of reaction R3
ΔT	Pyrolysis range of reaction R3

CRediT authorship contribution statement

Tássia L.S. Quaresma: Writing – review & editing, Writing – original draft, Visualization, Validation, Software, Methodology, Investigation, Formal analysis, Data curation, Conceptualization. **Tristan Hehnen:** Writing – review & editing, Validation, Conceptualization. **Lukas Arnold:** Writing – review & editing, Validation, Supervision, Software, Resources, Project administration, Methodology, Funding acquisition, Conceptualization.

Data and software availability

The data is publicly available in: https://doi.org/10.5281/zenodo.12804448.

Declaration of competing interest

The authors declare that they have no known competing financial interests or personal relationships that could have appeared to influence the work reported in this paper.

Acknowledgements

We gratefully acknowledge the computing time granted through the project on the CoBra-system, funded by the German Federal Ministry of Education and Research with the grant number 13N15497. This research was partially funded by the German Federal Ministry of Education and Research with the grant number 13N15497.

Data availability

The data is publicly available in: https://doi.org/10.5281/zenodo.12804448.

References

[1] Thomas Rogaume, Thermal decomposition and pyrolysis of solid fuels: Objectives, challenges and modelling, Fire Saf. J. 106 (2019) 177–188, http://dx.doi.org/10.1016/j.firesaf.2019.04.016.

[2] Karen De Lannoye, Corinna Trettin, Alexander Belt, E.A. Reinecke, Roland Goertz, Lukas Arnold, The influence of experimental conditions on the mass loss for TGA in fire safety science, Fire Saf. J. 144 (2024) 104079, http://dx.doi.org/10.1016/j.firesaf.2023.104079.

[3] Ilya M. Sobol, Global sensitivity indices for nonlinear mathematical models and their Monte Carlo estimates, Math. Comput. Simulation 55 (1–3) (2001) 271–280, http://dx.doi.org/10.1016/S0378-4754(00)00270-6.

[4] Jonathan Feinberg, Hans Petter Langtangen, Chaospy: An open source tool for designing methods of uncertainty quantification, J. Comput. Sci. 11 (2015) 46–57, http://dx.doi.org/10.1016/j.jocs.2015.08.008.

[5] Tatyana A. Bolshova, Ilya E. Gerasimov, Andrey G. Shmakov, Oleg P. Korobeinichev, Combustion of spherical PMMA samples in still air simulated using a skeletal chemical kinetic mechanism, Fire Saf. J. 138 (2023) 103807, http://dx.doi.org/10.1016/j.firesaf.2023.103807.

[6] Izabella Vermesi, Nils Roenner, Paolo Pironi, Rory M. Hadden, Guillermo Rein, Pyrolysis and ignition of a polymer by transient irradiation, Combust. Flame 163 (2016) 31–41, http://dx.doi.org/10.1016/j.combustflame.2015.08.006.

[7] Gregory J. Fiola, Dushyant M. Chaudhari, Stanislav I. Stoliarov, Comparison of pyrolysis properties of extruded and cast poly (methyl methacrylate), Fire Saf. J. 120 (2021) 103083, http://dx.doi.org/10.1016/j.firesaf.2020.103083.

[8] Patrick Lauer, Tristan Hehnen, Fabian Brännström, Lukas Arnold, Corinna Trettin, Karen De Lannoye, Pyrolysis model data set contribution for the Macfp workshop April 2021 - dataset, 2021, http://dx.doi.org/10.5281/zenodo.470457, Zenodo.

[9] Patrick Lauer, Lukas Arnold, Fabian Brännström, Inverse modelling of pyrolization kinetics with ensemble learning methods, Fire Saf. J. 136 (2023) 103744, http://dx.doi.org/10.1016/j.firesaf.2023.103744.

[10] M. Ferriol, A. Gentilhomme, M. Cochez, N. Oget, J.L. Mieloszynski, Thermal degradation of poly (methyl methacrylate)(PMMA): modelling of DTG and TG curves, Polym. Degrad. Stab. 79 (2) (2003) 271–281, http://dx.doi.org/10.1016/S0141-3910(02)00291-4.

[11] Tristan Hehnen, Lukas Arnold, PMMA pyrolysis simulation – from micro- to real-scale, Fire Saf. J. 141 (2023) 103926, http://dx.doi.org/10.1016/j.firesaf.2023.103926.

[12] W.R. Zeng, S.F. Li, Wan Ki Chow, Review on chemical reactions of burning poly (methyl methacrylate) PMMA, J. Fire Sci. 20 (5) (2002) 401–433, http://dx.doi.org/10.1177/0734904102020005482.

[13] B.J. Holland, J.N. Hay, The effect of polymerisation conditions on the kinetics and mechanisms of thermal degradation of PMMA, Polym. Degrad. Stab. 77 (3) (2002) 435–439, http://dx.doi.org/10.1016/S0141-3910(02)00100-3.

[14] Matthew DiDomizio, Mark McKinnon, Impact of specimen preparation method on thermal analysis testing and derived parameters, in: Symposium on Obtaining Data for Fire Growth Models, ASTM International, 2023, pp. 64–87, http://dx.doi.org/10.1520/STP164220210106.

[15] David Morrisset, Simón Santamaria, Rory Hadden, Richard Emberley, Implications of data smoothing on experimental mass loss rates, Fire Saf. J. 131 (2022) 103611, http://dx.doi.org/10.1016/j.firesaf.2022.103611.

[16] Sergey Vyazovkin, Alan K. Burnham, José M. Criado, Luis A. Pérez-Maqueda, Crisan Popescu, Nicolas Sbirrazzuoli, ICTAC kinetics committee recommendations for performing kinetic computations on thermal analysis data, Thermochim. Acta 520 (1–2) (2011) 1–19, http://dx.doi.org/10.1016/j.tca.2011.03.034.

[17] Morgan J. Hurley, Daniel T. Gottuk, John R. Hall Jr., Kazunori Harada, Erica D. Kuligowski, Milosh Puchovsky, John M. Watts Jr., Christopher J. Wieczorek, et al., SFPE Handbook of Fire Protection Engineering, Springer, 2015.

[18] Alexandra Viitanen, Simo Hostikka, Jukka Vaari, CFD simulations of fire propagation in horizontal cable trays using a pyrolysis model with stochastically determined geometry, Fire Technol. 58 (5) (2022) 3039–3065, http://dx.doi.org/10.1007/s10694-022-01291-6.

[19] T. Nyazika, M. Jimenez, F. Samyn, S. Bourbigot, Pyrolysis modeling, sensitivity analysis, and optimization techniques for combustible materials: A review, J. Fire Sci. 37 (4–6) (2019) 377–433, http://dx.doi.org/10.1177/0734904119852740.

[20] P. Lauer, T. Hehnen, C. Trettin, F. Brännström, L. Arnold, Role of the cost function for material parameter estimation, in: Fire and Evacuation Modelling Technical Conference, 2020, http://dx.doi.org/10.5281/zenodo.4007595.

[21] I. Leventon, B. Batiot, M. Bruns, S. Hostikka, Y. Nakamura, P. Reszka, T. Rogaume, S. Stoliarov, Measurement and computation of fire phenomena (MaCFP) - condensed phase material database (MATL-DB), 2023, https://github.com/MaCFP/matl-db/tree/master/PMMA/Material_Properties, Commit: 2393d51.

[22] Toshimi Hirata, Takashi Kashiwagi, James E. Brown, Thermal and oxidative degradation of poly (methyl methacrylate): weight loss, Macromolecules 18 (7) (1985) 1410–1418, http://dx.doi.org/10.1021/ma00149a010.

[23] Lewis E. Manring, Thermal degradation of poly (methyl methacrylate). 2. Vinyl-terminated polymer, Macromolecules 22 (6) (1989) 2673–2677, http://dx.doi.org/10.1021/ma00196a024.

[24] Lewis E. Manring, Dotsevi Y. Sogah, Gordon M. Cohen, Thermal degradation of poly (methyl methacrylate). 3. Polymer with head-to-head linkages, Macromolecules 22 (12) (1989) 4652–4654, http://dx.doi.org/10.1021/ma00202a048.

[25] Takashi Kashiwagi, Atsushi Inaba, James E. Brown, Koichi Hatada, Tatsuki Kitayama, Eiji Masuda, Effects of weak linkages on the thermal and oxidative degradation of poly (methyl methacrylates), Macromolecules 19 (8) (1986) 2160–2168, http://dx.doi.org/10.1021/ma00162a010.

[26] Dushyant M. Chaudhari, Gregory J. Fiola, Stanislav I. Stoliarov, Experimental analysis and modeling of buoyancy-driven flame spread on cast poly (methyl methacrylate) in corner configuration, Polym. Degrad. Stab. 183 (2021) 109433, http://dx.doi.org/10.1016/j.polymdegradstab.2020.109433.

[27] Yan Ding, Isaac T. Leventon, Stanislav I. Stoliarov, An analysis of the sensitivity of the rate of buoyancy-driven flame spread on a solid material to uncertainties in the pyrolysis and combustion properties. Is accurate prediction possible? Polym. Degrad. Stab. 214 (2023) 110405, http://dx.doi.org/10.1016/j.polymdegradstab.2023.110405.

[28] Nicolas Bal, Guillermo Rein, Numerical investigation of the ignition delay time of a translucent solid at high radiant heat fluxes, Combust. Flame 158 (6) (2011) 1109–1116, http://dx.doi.org/10.1016/j.combustflame.2010.10.014.

[29] Richard E. Lyon, Richard N. Walters, Pyrolysis combustion flow calorimetry, J. Anal. Appl. Pyrolysis (ISSN: 0165-2370) 71 (1) (2004) 27–46, http://dx.doi.org/10.1016/S0165-2370(03)00096-2, URL https://www.sciencedirect.com/science/article/pii/S0165237003000962, Practical Applications of Analytical Pyrolysis (special section).

[30] Joshua D. Swann, Yan Ding, Mark B. McKinnon, Stanislav I. Stoliarov, Controlled atmosphere pyrolysis apparatus II (CAPA II): A new tool for analysis of pyrolysis of charring and intumescent polymers, Fire Saf. J. (ISSN: 0379-7112) 91 (2017) 130–139, http://dx.doi.org/10.1016/j.firesaf.2017.03.038, URL https://www.sciencedirect.com/science/article/pii/S0379711217300541, Fire Safety Science: Proceedings of the 12th International Symposium.

[31] Tássia L.S. Quaresma, Tristan Hehnen, Lukas Arnold, Sensitivity analysis for an effective transfer of estimated material properties from cone calorimeter to horizontal flame spread simulations, Fire Saf. J. (2024) 104116, http://dx.doi.org/10.1016/j.firesaf.2024.104116.

[32] K. McGrattan, S. Hostikka, J. Floyd, R. McDermott, M. Vanella, Fire Dynamics Simulator (version FDS6.7.6-810-ge59f90f-HEAD) – User's Guide, US Department of Commerce, Technology Administration, NIST, 2005, http://dx.doi.org/10.6028/NIST.SP.1019.

[33] Kevin McGrattan, Simo Hostikka, Randall McDermott, Jason Floyd, Craig Weinschenk, Kristopher Overholt, Fire dynamics simulator technical reference guide volume 1: mathematical model, NIST Spec. Publ. 1018 (1) (2013) 175.

[34] NIST, FDS validation repository on Github, 2023, https://github.com/firemodels/fds/tree/master/Validation/NIST_NRC_Parallel_Panels, Commit: 300ee40.

[35] Jing Li, Stanislav I. Stoliarov, Measurement of kinetics and thermodynamics of the thermal degradation for non-charring polymers, Combust. Flame 160 (7) (2013) 1287–1297, http://dx.doi.org/10.1016/j.combustflame.2013.02.012.

[36] NIST, FDS validation repository, NIST NRC parallel panels, PMMA_60_kW_1_cm.fds; Github, 2023, https://github.com/firemodels/fds/blob/300ee407ca64757098623ccc7ede12ae548137f8/Validation/NIST_NRC_Parallel_Panels/FDS_Input_Files/PMMA_60_kW_1_cm.fds, Commit: 300ee40.

[37] Andrea Saltelli, Ksenia Aleksankina, William Becker, Pamela Fennell, Federico Ferretti, Niels Holst, Sushan Li, Qiongli Wu, Why so many published sensitivity analyses are false: A systematic review of sensitivity analysis practices, Environ. Model. Softw. 114 (2019) 29–39, http://dx.doi.org/10.1016/j.envsoft.2019.01.012.

[38] Mark B. McKinnon, Evaluation of uncertainty in direct measurement for parameterization of pyrolysis models, Part I: Thermal analysis, Fire Saf. J. 141 (2023) 104000, http://dx.doi.org/10.1016/j.firesaf.2023.104000.

[39] Hamza Jamil, Fabian Brännström, Intrusive and non-intrusive uncertainty quantification methodologies for pyrolysis modeling, Fire Saf. J. 143 (2024) 104060, http://dx.doi.org/10.1016/j.firesaf.2023.104060.

[40] Andrea Saltelli, Marco Ratto, Terry Andres, Francesca Campolongo, Jessica Cariboni, Debora Gatelli, Michaela Saisana, Stefano Tarantola, Global Sensitivity Analysis: The Primer, John Wiley & Sons, 2008.

[41] O. Korobeinichev, M. Gonchikzhapov, A. Tereshchenko, I. Gerasimov, A. Shmakov, A. Paletsky, Al. Karpov, An experimental study of horizontal flame spread over PMMA surface in still air, Combust. Flame 188 (2018) 388–398, http://dx.doi.org/10.1016/j.combustflame.2017.10.008.

[42] L. Jiang, C.H. Miller, M.J. Gollner, J. Sun, Sample width and thickness effects on horizontal flame spread over a thin PMMA surface, Proc. Combust. Inst. 36 (2) (2017) 2987–2994, http://dx.doi.org/10.1016/j.proci.2016.06.157.